Journal of Magnetic Resonance 299 (2019) 168–175

Contents lists available at ScienceDirect

Journal of Magnetic Resonance

journal homepage: www.elsevier.com/locate/jmr

Larmor frequency in heterogeneous media

Valerij G. Kiselev

Dept. of Radiology, Medical Physics, Medical Center, Faculty of Medicine, University of Freiburg, Freiburg, Germany

ARTICLE INFO

Article history:
Received 14 October 2018
Revised 28 November 2018
Accepted 13 December 2018
Available online 15 December 2018

Keywords:
Microstructure
Magnetic susceptibility
Porous media
Larmor frequency
Lorentz cavity

ABSTRACT

High-precision signal phase measurements ignited an ongoing discussion of the microstructural correlates of the Larmor frequency shift of water in biological tissues. In a broader context, this is the question about the averaged precession frequency in magnetically heterogenous, in particular, porous media. In this study, the Larmor frequency shift is found analytically for water filling connected pore space between NMR-invisible magnetized inclusions with a constant magnetic susceptibility tensor. The magnetic microstructure that encompasses the inclusions' shape and their spatial arrangement is arbitrary as well as the inclusions' magnetic susceptibility tensor. The result is limited to the case of effectively fast diffusion of water molecules. In this limit, the effect of magnetic microstructure on the Larmor frequency shift is represented by only five relevant parameters in the general case and by a single parameter in the case of axially symmetric microstructure. This single parameter enters the dependence of the Larmor frequency on the sample orientation relative to the main magnetic field in the previously performed experiments. The result can help interpreting known experimental data and developing realistic models of biological tissues.

© 2018 Elsevier Inc. All rights reserved.

1. Introduction

Precise measurement of the signal phase in the human brain at high magnetic field [1–3] reanimated the interest in calculating the Larmor frequency shift in media with heterogeneous magnetic properties, in particular brain white matter with the account for the distinct magnetic susceptibility of myelin. In the focus of intensive discussion, this problem has decoupled from its original biomedical context. From the physics point of view, the challenge is to calculate the measurable phase of NMR signal acquired in a medium consisting of an NMR-reporting liquid (referred to as water in what follows) and numerous microscopic NMR-invisible inclusions with a magnetic susceptibility different from that of water (those can represent biological cells), Fig. 1. Considering such a medium as porous material, all inclusions form the matrix, while the signal originates from the water-filled pore space. In view of the currently increasing interest in biomedical applications, the biology-inspired terminology is used hereafter rather than that of porous media.

A non-trivial effect of the medium microstructure originates from the proximate environment of each NMR-reporting spin. In this region, the standard macroscopic averaging does not work, since the signal-contributing spins "resolve" the microstructure, which results in a distinct contribution of the proximate region to the local time-averaged magnetic field experienced by the spins. In particular, fast water diffusion between isotropic microscopic inclusions results in zero contribution of this region to the averaged field. The effect is akin to the field averaging on the molecular scale, where the local time-averaged field in isotropic liquids is zero, as it is taken into account by the classic Lorentz sphere construction [4–6]. In analogy with this construction, the zero effect of the proximate microscopic inclusions can be described as a Lorentz sphere as it was proposed when considering the frequency shift in blood [7,8]. This sphere is effective on a scale that is larger than that of inclusions to account for a statistically large number of them, but smaller than the macroscopic scale of the whole sample or an imaging voxel. In what follows, this intermediate scale will be called *mesoscopic* in line with the terminology accepted in physics.

A still ongoing discussion was initiated by the idea to match the shape of the mesoscopic Lorentz cavity to the microscopic magnetic architecture in structured media such as brain white matter [9,10]. Further development of this idea resulted in white matter modeled with magnetic inclusions with both the isotropic and elongated shapes; inclusions of different types contribute *additively* to the Larmor frequency offset [11–13], whereas each type involves the Lorentz cavity construction with the shape matching its geometry, spherical or cylindrical, respectively. The additive contribution of different inclusions has been recognized as the limit of their low volume fraction and independent distributions

E-mail address: kiselev@ukl.uni-freiburg.de

https://doi.org/10.1016/j.jmr.2018.12.008
1090-7807/© 2018 Elsevier Inc. All rights reserved.

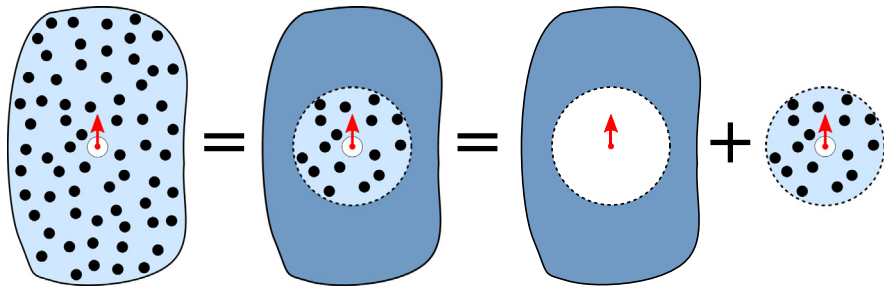

Fig. 1. A sample with a microscopic magnetic structure and the decomposition of its magnetization for calculating the magnetic field at the position of an NMR-reporting spin (red arrow). The heterogeneous magnetization is shown as inclusions (black dots) with a magnetic susceptibility different from that of the surrounding fluid (light blue). The first equality: The sample can be divided into a far and a spherical near region, the *mesoscopic sphere* (the sphere size is greatly exaggerated in the image). The far region contributes a field proportional to its average (homogenized) susceptibility (darker blue). The second equality: The field at the spin's position is the sum of two contributions induced by the far region without the mesoscopic sphere, $\mathbf{B}^{\text{macro}}$ and the mesoscopic sphere, Eq. (6). The field from within the sphere, $\mathbf{B}^{\text{meso}}$, needs to be calculated given the medium microarchitecture. The small empty sphere stands for the classical Lorentz sphere in the NMR-reporting fluid. (For interpretation of the references to color in this figure legend, the reader is referred to the web version of this article.)

[14], which is a serious confounding factor for biological applications.

A further challenge was posed by the anisotropic magnetic susceptibility of myelin [15,16,11,17]. Projected on the present consideration, it implies an *intrinsic* anisotropy of the material of magnetic susceptibility inclusions in addition to their *structural* anisotropy considered above. Sukstanskii and Yablonskiy developed a theory to account for the combined effect of both types of anisotropy. To find the mean field outside the impermeable inclusions, they subtracted the intra-inclusion field from the macroscopically averaged magnetic field [12,13]. On this way, they had to assume the ellipsoidal shape of inclusions and kept using the approximation of their low volume fraction.

Summarizing the state of the art, it remains a challenge to find the microstructural correlates of the anisotropic precession frequency in white matter [16,18–21] with account for real tissue structure characterized by a high density of cells of distinct shapes and magnetic properties.

In this work, I develop a theory for the case of fast water diffusion in connected space outside magnetized inclusions of *arbitrary density and geometry*. Other inclusions' properties are treated in the simplest possible way. Namely, the inclusions are NMR-invisible and have all the same *position-independent* anisotropic magnetic susceptibility. A way to more realistic models of white matter is discussed at the end of this paper. The main result is a formula for the Larmor frequency offset in which the medium's magnetic microarchitecture enters via the *correlation function* of magnetized inclusions, Eq. (15) below; this formula generalizes the recent result for the case of isotropic magnetic susceptibility [22]. In the most general case, the frequency offset depends on five relevant parameters of the correlation function and does not depend on an infinite set of other parameters specifying its functional form. In the case of axially symmetric media, Eq. (18) below, there is a single relevant parameter representing the medium microarchitecture. This result is applied to possible experiments with samples rotated in the main field in the spirit of those performed with extracted nerve tissues [19,16,21].

2. Methods (Setting the scene)

The above described medium consists of NMR-invisible magnetized inclusions occupying the fraction ζ of the sample volume. The water-filled space between inclusions is connected (no traps for water). The union of all inclusions is described by an indicator function $v(\mathbf{r})$ that is unity inside any inclusion and zero otherwise. The inclusions' material is characterized by anisotropic magnetic susceptibility described by a tensor χ_{ab}, where a, b label the three spatial components of vectors and tensors. This material is considered to be non-ferromagnetic, which means that $|\chi_{ab}| \ll 1$. This condition enables finding the macroscopic inclusions' magnetization in the cgs system as

$$M_a = \chi_{ab} B_{0,b}, \tag{1}$$

where $B_{0,b}$ is the b-component of the main field and the Einstein's convention about the summation over repeating indices is assumed throughout this paper. To focus on the effect of microstructure, the magnetic susceptibility is considered relative to water. Correspondingly, the magnetic field calculated below is reduced by the field induced within the sample homogeneously filled with water without inclusions. This background contribution should be taken into account for real measurements.

The additional macroscopic magnetic field induced by the inclusions takes the form

$$\Delta B_a(\mathbf{r}) = \int \mathrm{d}^3 r_0\, \mathcal{Y}_{ab}(\mathbf{r} - \mathbf{r}_0)\, M_b(\mathbf{r}_0), \tag{2}$$

where $\mathcal{Y}_{ab}$ is the elementary dipole field,

$$\mathcal{Y}_{ab}(\mathbf{r}) = \frac{3\,\hat{r}_a \hat{r}_b - \delta_{ab}}{r^3} \tag{3}$$

with the hat denoting unit vectors, $\hat{r}_a = r_a/r$ and δ_{ab} the Kronecker delta, which is unity for $a = b$ and zero otherwise. Since Eq. (2) has the form of a convolution, the field can be efficiently calculated in the Fourier domain,

$$\Delta B_a(\mathbf{k}) = \mathcal{Y}_{ab}(\mathbf{k}) M_b(\mathbf{k}). \tag{4}$$

Note that the same root letters are used throughout this paper for the original and Fourier-transformed quantities; the argument is always given explicitly to avoid confusion. The Fourier transform of the dipole field, Eq. (3), takes the following form in the cgs system (see e.g. [23,24]):

$$\mathcal{Y}_{ab}(\mathbf{k}) = 4\pi \left(\frac{\delta_{ab}}{3} - \frac{k_a k_b}{k^2} \right). \tag{5}$$

This expression takes into account the field of the Lorentz sphere for water molecules, $8\pi\delta_{ab}/3$ [5,6], which is discussed in more detail below.

The time-averaged magnetic field experienced by a water proton deviates from the value given by Eq. (2) because the condition of averaging over the molecular scale does not fulfill for the closest environment of the spin. Following the original idea of Lorentz [4], the effect of this environment should be considered with account for its microscopic structure and dynamics. In isotropic liquids such as water, this leads to the zero average field from the nearest

environment, which is effectively taken into account by using the macroscopic Eq. (2) with an infinitesimal spherical cavity in $\mathbf{M}(\mathbf{r})$, the Lorentz sphere [5,6], which is already accounted for in Eq. (5).

In media with microscopic structures, many orders of magnitude coarser than the molecular dimensions, Eq. (2) is valid on the microscopic scale. However, the effect of heterogeneous field should be specifically averaged to yield the overall Larmor frequency from the whole macroscopic sample (or an MRI voxel). This averaging occurs on the mesoscopic scale, which is coarser than the microscopic one, but much finer than the macroscopic sample size. Performing the necessary averaging on this scale is the overarching goal of the present study.

This goal is approached by replicating the original idea of Lorentz on the mesoscopic scale [7,8]: The whole sample is subdivided in a near and a far region relative to any considered NMR-reporting spin. While the far region contributes the field according to the macroscopically averaged medium parameters, the field in the near region should be calculated with account for the medium microscopic structure and the diffusive motion of water molecules. It is convenient to select the near region in the form of a sphere, Fig. 1. This sphere is called the *mesoscopic sphere* in what follows. Its size is much smaller than the sample dimensions, but large enough to enable a smooth transition from the local environment of a given proton to the macroscopically averaged medium properties. In other words, the sphere size is large enough to include a statistically representative portion of the medium. This study is focused on the case of fast diffusion, which means that the diffusion length in each direction is very large on the microscopic scale for the typical time of the signal acquisition, still it is well below the size of the mesoscopic sphere. Deviations from this condition for isotropic media are discussed elsewhere [22,25].

Accordingly to the sample decomposition shown in Fig. 1, the average deviation from the main field, $\Delta\bar{\mathbf{B}}$, experienced by a proton consists of two terms,

$$\Delta\bar{\mathbf{B}} = \mathbf{B}^{\text{macro}} + \mathbf{B}^{\text{meso}}, \tag{6}$$

where $\mathbf{B}^{\text{macro}}$ is the field created by a macroscopically homogeneous sample of the given shape with a small spherical cavity in the place of the mesoscopic sphere around the reporting spin and $\mathbf{B}^{\text{meso}}$ is the field of the mesoscopic sphere. Finding the latter is the goal of the subsequent calculations.

3. Results

3.1. Frequency offset inside mesoscopic sphere

The local Larmor frequency offset within the mesoscopic sphere is given by the longitudinal projection of the susceptibility-induced magnetic field, $\mathbf{B}^{\text{meso}}(\mathbf{r})$,

$$\Omega(\mathbf{r}) = \gamma n_a B_a^{\text{meso}}(\mathbf{r}), \tag{7}$$

where $\mathbf{n} = \mathbf{B}_0/B_0$ is the unit vector in the direction of the main magnetic field. The mesoscopic field varies over the characteristic length defined by the medium structure. The case of fast diffusion considered here implies that during the measurement the typical spin samples a large, statistically representative portion of the medium. In this case, called the diffusion or motional narrowing, the reported Larmor frequency, $\overline{\Omega}$, is defined by the *spatial averaging* of the local frequency, $\Omega(\mathbf{r})$, over the space occupied by water,

$$\overline{\Omega} = \int \frac{\mathrm{d}^3 r}{(1-\zeta)V}\, \Omega(\mathbf{r})\,[1 - v(\mathbf{r})]. \tag{8}$$

While the integration here is performed over the whole volume of mesoscopic sphere, V, the inclusions' volume is excluded by the indicator function $1 - v(\mathbf{r})$ with the denominator, $(1-\zeta)V$, written for the normalization on the water volume (cf. Eq. 12 in [22]).

The field within the sphere, $\Omega(\mathbf{r})$, is found according to Eq. (2) with the magnetization from Eq. (1). To simplify the analysis, the magnetic susceptibility tensor, χ_{ab}, is assumed to be equal for all inclusions within the mesoscopic sphere, which enables delegating the spatial dependence of magnetic susceptibility to the indicator function of inclusions, $v(\mathbf{r})$. In the real world this can describe a porous medium made with a homogeneously magnetized matrix. This assumption does not preclude slow variations of χ_{ab} over the macroscopic scale of the sample. A way beyond this limitation is discussed in Section 4. This results in

$$\frac{\overline{\Omega}}{\Omega_0} = \int \frac{\mathrm{d}^3\mathbf{r}_1}{(1-\zeta)V}\, \mathrm{d}^3\mathbf{r}_0\,[1 - v(\mathbf{r}_1)]\, n_a \mathcal{Y}_{ab}(\mathbf{r}_1 - \mathbf{r}_0)\chi_{bc} n_c\, v(\mathbf{r}_0), \tag{9}$$

where $\Omega_0 = \gamma B_0$ is the nominal Larmor frequency. The first term inside the brackets gives rise to the integral over $\mathbf{r}_1$, which is proportional to the field induced by a homogeneously magnetized sphere (the source and the measurement points in $\mathcal{Y}_{ab}(\mathbf{r}_1 - \mathbf{r}_0)$ are interchanged for this interpretation). Since the elementary dipole field, Eq. (5), takes into account the field of the Lorentz sphere, the contribution of the first term is identically zero. In the remaining integral, which is bilinear in $v(\mathbf{r})$, the variable $\mathbf{r}_1$ is substituted with $\mathbf{r}_0 + \mathbf{r}$, which gives

$$\frac{\overline{\Omega}}{\Omega_0} = -\int \frac{\mathrm{d}^3\mathbf{r}\,\mathrm{d}^3\mathbf{r}_0}{(1-\zeta)V}\, v(\mathbf{r}_0 + \mathbf{r})\, v(\mathbf{r}_0) n_a \mathcal{Y}_{ab}(\mathbf{r})\chi_{bc} n_c, \tag{10}$$

For a fixed $\mathbf{r}$, the integration over $\mathbf{r}_0$ is performed over the overlap of two mesoscopic spheres with radius R, $r_0 < R$ and $|\mathbf{r}_0 + \mathbf{r}| < R$, Fig. 2. The overlap volume is large, close to the volume of the mesoscopic sphere for the relevant values of $\mathbf{r}$, which are of the order of magnitude of the medium correlation length. Given such a large (not necessarily spherical) overlap volume, the $\mathbf{r}_0$-integrated product $v(\mathbf{r}_0 + \mathbf{r})\, v(\mathbf{r}_0)$ gives rise to the density-density *correlation function* of the inclusions,

$$\Gamma(\mathbf{r}) = \int \frac{\mathrm{d}^3\mathbf{r}_0}{V}\, v(\mathbf{r}_0 + \mathbf{r})\, v(\mathbf{r}_0) - \zeta^2, \tag{11}$$

where ζ appears as the volume mean of $v(\mathbf{r})$. The integral from this expression is substituted in Eq. (10), where the ζ^2 integrated with $\mathcal{Y}_{ab}(\mathbf{r})$ gives zero by the same reason as above taking into account

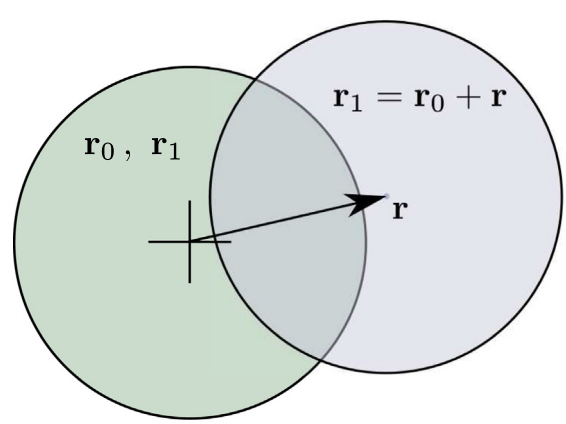

Fig. 2. Illustration of the integration variable change on the transition from Eq. (9) to Eq. (10). The original integration over $\mathbf{r}_0$ and $\mathbf{r}_1$ spans the sphere centered around the origin (the cross). The substitution $\mathbf{r}_1 = \mathbf{r}_0 + \mathbf{r}$ shifts this sphere by the vector $\mathbf{r}$, but the original limits on the $\mathbf{r}_1$ integration reduces the $\mathbf{r}_0$ integration volume to the intersection of the two spheres. This volume is large enough to provide for the averaging that gives the correlation function, Eq. (11). This condition is violated for large $\mathbf{r}$ for which the intersection collapses, but such values are not relevant because $\Gamma(\mathbf{r})$ is essentially nonzero only for r much smaller than the sphere size.

that the $\mathbf{r}$ integration is performed over the sphere of the radius $2R$. The final expression thus takes the form

$$\frac{\overline{\Omega}}{\Omega_0} = -\frac{1}{1-\zeta}\int \mathrm{d}^3\mathbf{r}\, n_a \mathcal{Y}_{ab}(\mathbf{r})\chi_{bc} n_c\, \Gamma(\mathbf{r}). \tag{12}$$

For further analysis, it is convenient to formulate this result in terms of the Fourier-transformed quantities. Straightforward transformation of Eq. (11) gives

$$\Gamma(\mathbf{k}) = \frac{v(\mathbf{k})\, v(-\mathbf{k})}{V}, \tag{13}$$

where $\Gamma(\mathbf{k})$ is discontinuous at $\mathbf{k} = 0$; its value at this point is zero, which is easy to show by integrating Eq. (11) over $\mathbf{r}$. The final result in the Fourier domain takes the form

$$\frac{\overline{\Omega}}{\Omega_0} = -\frac{1}{1-\zeta}\int \frac{\mathrm{d}^3 k}{(2\pi)^3}\, n_a \mathcal{Y}_{ab}(\mathbf{k})\chi_{bc} n_c\, \Gamma(\mathbf{k}), \tag{14}$$

where the elementary dipole field, $\mathcal{Y}_{ab}(\mathbf{k})$, is defined in Eq. (5). Here the correlation function is the only quantity that depends on the length of vector $\mathbf{k}$. The radial integration can be performed resulting in the expression

$$\frac{\overline{\Omega}}{\Omega_0} = -\frac{1}{1-\zeta}\int \mathrm{d}^2\hat{k}\, n_a \mathcal{Y}_{ab}\left(\hat{k}\right)\chi_{bc} n_c\, \overline{\Gamma}\left(\hat{k}\right), \tag{15}$$

where the hats are written to underscore the exclusive dependence of all quantities on the orientation of $\hat{k} = \mathbf{k}/k$, the integration is performed over the full solid angle in k-space and

$$\overline{\Gamma}\left(\hat{k}\right) = \frac{1}{(2\pi)^3}\int_0^\infty dk k^2 \Gamma(\mathbf{k}). \tag{16}$$

3.1.1. Relevant medium parameters

It is worth noticing that the medium's magnetic microarchitecture is represented in the observable frequency shift by only five relevant coefficients. This follows from the observation that the elementary dipole field, Eq. (5) is a trace-free tensor of the second rank build of the unit vector $\hat{k}$. There is one-to-one correspondence between the components of such tensors and the spherical harmonics, $Y_\ell^m\left(\hat{k}\right)$, of the order $\ell = 2$ with explicit formulas given in Appendix A. In other words, $\mathcal{Y}_{ab}\left(\hat{k}\right)$ and the expression $n_a \mathcal{Y}_{ab}\left(\hat{k}\right)\chi_{bc} n_c$ in Eq. (15) are linear combinations of spherical harmonics $Y_2^m\left(\hat{k}\right)$. Therefore, the integration in Eq. (15) performs a projection of all terms in the spherical harmonic expansion of $\overline{\Gamma}\left(\hat{k}\right)$ onto the subspace with $\ell = 2$; the terms with $\ell \neq 2$ do not contribute. Since $\overline{\Gamma}\left(\hat{k}\right)$ is real according to Eq. (13), the expansion coefficients C_2^m in front of $Y_2^m\left(\hat{k}\right)$ obey the condition $C_2^{m*} = (-1)^m C_2^{-m}$. The five relevant real-valued parameters are defined by the complex-valued coefficients C_2^2, C_2^1 and the real-valued C_2^0.

Note that for the case of structurally isotropic media, $\overline{\Gamma}\left(\hat{k}\right)$ is a constant and all expansion coefficients in front of Y_2^m are zero. The mesoscopic sphere thus does not contribute to the average field. In other words, it can be treated as an extension of the classical molecular Lorentz sphere on the mesoscopic scale [7,8].

3.2. The case of axial symmetry

The axial symmetry in the present context can refer to two different quantities. First, it is the *magnetic* axial symmetry, which implies that the susceptibility tensor χ_{ab} has the eigenvalues $\chi_\perp, \chi_\perp, \chi_\parallel$. Secondly, it is the *structural* axial symmetry, which refers to the symmetry of the correlation function $\overline{\Gamma}\left(\hat{k}\right)$. While these properties can be thought independent, this section deals with the most realistic case of the full (magneto-structural) axial symmetry with coinciding magnetic and structural symmetry axes. For brevity, this case will be simply referred to as the "axial symmetry".

When conducting experiments with such media, it makes sense to select samples of cylindrical shape co-axial with the symmetry axis, which is assumed in Section 3.2.3 below. Such a setup serves as a (strongly simplified) model of experiments performed with excised segments of nerves [19,21,20]. The aim of this section is to find the frequency shift for such a sample arbitrarily orientated relative to the main field.

3.2.1. Single relevant medium parameter

The structural axial symmetry implies that $\overline{\Gamma}\left(\hat{k}\right)$ does not depend on the azimuthal angle, φ, in the properly chosen reference frame. Therefore, the expansion of $\overline{\Gamma}\left(\hat{k}\right)$ in spherical harmonics contains only terms with $m = 0$. Since the only further $\hat{k}$-dependent factor in Eq. (15) is $\mathcal{Y}_{ab}\left(\hat{k}\right)$, which is a linear combination of Y_2^m as discussed in Section 3.1.1, the only contributing components of $\overline{\Gamma}\left(\hat{k}\right)$ is proportional to Y_2^0,

$$\overline{\Gamma}\left(\hat{k}\right) = C_2^0 Y_2^0\left(\hat{k}\right) + \ldots, \tag{17}$$

where the dotted terms do not contribute to the frequency shift. The coefficient C_2^0 is thus the only relevant parameter in the frequency shift representing the microarchitecture of a medium with axial symmetry.

3.2.2. Frequency offset inside the mesocopic sphere

The frequency offset in (fully) axially symmetric media can only depend on the tilt angle, θ, between the medium principal axis and the main field. Straightforward calculation of the matrix-vector product $n_a \mathcal{Y}_{ab}\left(\hat{k}\right)\chi_{bc} n_c$ in Eq. (15) (Appendix B) results in the following expression for the mean field inside the mesoscopic sphere

$$\frac{\overline{\Omega}}{\Omega_0} = \frac{8\pi^2}{3\sqrt{5\pi}}\frac{C_2^0}{1-\zeta}\left[\left(2\chi_\parallel + \chi_\perp\right)\cos^2\theta - \chi_\perp\right]. \tag{18}$$

The observed frequency shift is found by the addition of the macroscopic contribution defined by $\mathbf{B}^{\mathrm{macro}}$ for the overall cylindrical shape with the macroscopically averaged susceptibility tensor, $\zeta\chi_{ab}$ (the first term on the right-hand side of Eq. (6) with a graphical representation in Fig. 1). A straightforward calculation yields

$$\frac{\overline{\Omega}^{\mathrm{macro}}}{\Omega_0} = \frac{2\pi}{3}\zeta\left[\left(2\chi_\parallel + \chi_\perp\right)\cos^2\theta - \chi_\perp\right]. \tag{19}$$

3.2.3. Experiments with axially symmetric samples

The result expressed in Eq. (18) can be considered as a simplified model of experiments in which the signal phase was measured in excised segments of animal optic nerves as a function of the segment orientation relative to the main field [19,21]. In both experiments, the frequency shift created by the sample in the embedding fluid was used to find the overall sample-averaged magnetic susceptibility that was compared with the frequency shift inside the nerve. Luo et al. [19] interpreted the discovered anisotropy from the microstructural point of view; the sample was considered as consisting of isotropic and cylindrical magnetic susceptibility inclusions, either with a scalar (isotropic) magnetic susceptibility. As discussed above, this is a correct quantitative

description for inclusions with low volume fraction. Beyond this assumption, the decomposition in isotropic and cylindrical inclusion should be considered as an effective representation [26] of the more general result, Eq. (18).

Wharton and Bowtell [21] circumvented the lack of theoretical description for dense media by finding the microstructural contribution as the difference between the measured frequency shift and the traditional approach for the sample with anisotropic magnetic susceptibility. They described the difference as $f_R = A\sin^2\theta + b$, where A is due to the microstructure contribution and b to both the microstructure and the possible chemical exchange [27]. Since the traditional approach takes into account the sphere of Lorentz, the resulted frequency shift coincides with Eq. (19). The difference is therefore given by Eq. (18). Identifying the sample-averaged components of the susceptibility tensor, $\zeta\chi_\parallel$ and $\zeta\chi_\perp$, with $\chi_I + \chi_A$ and $\chi_I - \chi_A/2$ from Ref. [21], respectively, results in the following expression for the extra-axonal contribution, A_e, to the empirical coefficient A:

$$A_e = -\frac{8\pi^2}{\sqrt{5\pi}}\frac{C_2^0}{\zeta(1-\zeta)}\left(\chi_I + \frac{\chi_A}{2}\right)\gamma B_0 \tag{20}$$

in the cgs system; in the SI, which was used in Ref. [21], the factor 4π is absorbed in the correspondingly larger numerical values of magnetic susceptibilities.

The numerical value of coefficient A as found by Wharton and Bowtell resulted in an essential contribution to the frequency shift. As they showed by simulations in a realistic digital phantom obtained by translating properties of an excised optic nerve to the whole human brain white matter, both the quantitative susceptibility mapping [28,29] and the susceptibility tensor imaging [30] cannot quantify the white matter microstructure until the microstructural effects are taken into account in the data processing. This account, however, requires performing at least diffusion tensor imaging for the determination of the local fiber configuration [21,13,31].

3.3. Effectively two-dimensional media

Consider media in which the microstructure is translationally invariant in the third direction, while arbitrary in the cross-sectional plane. The correlation function in this case does not depend on the third coordinate, which implies the following form in the Fourier domain:

$$\Gamma(\mathbf{k}) = 2\pi\delta(k_3)\,\Gamma^{(2d)}(k_1, k_2), \tag{21}$$

where $\delta(k_3)$ is the Dirac delta-function and $\Gamma^{(2d)}$ the two-dimensional correlation function in the transverse cross-section of the mesoscopic sphere. This results in a universal form of the projection of $\overline{\Gamma}\left(\hat{k}\right)$ on $Y_2^0\left(\hat{k}\right)$ (Appendix C),

$$C_2^0 = -\frac{\sqrt{5\pi}}{4\pi}\zeta(1-\zeta), \tag{22}$$

which is completely determined by the inclusions' volume fraction being independent of other microstructural details. Note that the coefficient C_2^0 is negative in media with elongated microstructure as in the extreme example given by Eq. (22). In such media, $\Gamma(\mathbf{r})$ is elongated towards the cigar shape due to the stronger correlation along the principal axis. The Fourier transform, $\Gamma(\mathbf{k})$, is correspondingly closer to a disk-shaped form, which, along with the explicit form of Y_2^0, Eq. (A.3), leads to negative values of C_2^0.

In general, $\overline{\Gamma}\left(\hat{k}\right)$ has two other non-zero projections on $Y_2^{\pm 2}$, Eqs. (A.1) and (A.5) that are not universal being dependent on the specific form of $\Gamma^{(2d)}$. These projections are however absent for the axially symmetric media considered in Section 3.2. For such media, substitution of Eq. (22) in Eq. (18) results in the following contribution of the mesoscopic sphere to the frequency shift

$$\frac{\overline{\Omega}}{\Omega_0} = -\frac{2\pi}{3}\zeta\left[\left(2\chi_\parallel + \chi_\perp\right)\cos^2\theta - \chi_\perp\right]. \tag{23}$$

This expression is exactly opposite to the macroscopic contribution of a cylindrical sample Eq. (19), which results in the identical zero frequency shift for macroscopic samples with the overall microstructure-corresponding cylindrical shape (a bunch of cylinders). This is how the present general approach reproduces the well-known fact, which is obvious when the cylinder-shaped mesoscopic cavity is used instead of the sphere in this special case [9,10]. For arbitrary inclusions' geometry in the cross-sectional plane, the cancellation occurs only for the case of the main field parallel to the third axis. Technically, this follows from the absence of components with $m = \pm 2$ in the dipole field, Eq. (5).

3.4. Incorporation in the macroscopic picture

Consider the implementation of the main result, Eq. (15), in the description of the frequency shift in a macroscopically large object such as the human brain. The medium properties entering Eq. (15) become position dependent and the resulted frequency shift, $\overline{\Omega}(\mathbf{R})$, acquire a dependence on the macroscopic location $\mathbf{R}$. This macroscopic dependence is much slower than the variations on the microscopic scale, which preserves the above equations in which the integrals converge on the mesoscopic scale. When the Fourier transformation is involved, the variable, which is Fourier-conjugated to $\mathbf{R}$ (and denoted hereafter as $\mathbf{q}$) is much smaller than the mesoscopic variable $\mathbf{k}$ introduced above.

Using the decomposition of Eq. (6) (Fig. 1) and Eq. (15), the MRI-resolvable phase shift takes the form

$$\frac{\overline{\Omega}(\mathbf{R})}{\Omega_0} = n_a\left[\int \mathrm{d}^3\mathbf{R}_0\,\mathcal{Y}_{ac}(\mathbf{R}-\mathbf{R}_0)\overline{\chi}_{cb}(\mathbf{R}_0) + L_{ab}(\mathbf{R})\right]n_b, \tag{24}$$

where $\overline{\chi}_{bc}(\mathbf{R}_0)$ is the magnetic susceptibility tensor averaged on the mesoscopic scale at each macroscopic location. The tensor

$$L_{ab}(\mathbf{R}) = -\frac{1}{1-\zeta(\mathbf{R})}\int \mathrm{d}^2\hat{k}\,\mathcal{Y}_{ac}\left(\hat{k}\right)\chi_{cb}\,\overline{\Gamma}\left(\hat{k},\mathbf{R}\right) \tag{25}$$

adds to the field of classical Lorentz sphere, which is already accounted for in the term $\delta_{ab}/3$ in Eq. (5). Eq. (24) coincides in form with the generalized Lorentzian tensor approach [12,13], whereas the microstructural content of L_{ab}, Eq. (25), generalizes the case of sparse elliptical inclusions [12,13] to arbitrary inclusions' geometry with the connected space between them (in contrast to the present notations, the term $\delta_{ab}/3$ in that works was included in L_{ab}). The volume fraction and the correlation function in Eq. (24) acquire dependence on $\mathbf{R}$ according to the macroscopic variations in the medium properties.

The presence of a non-zero L_{ab} in structurally anisotropic media distorts the main assumption of quantitative susceptibility mapping [28,29] and the susceptibility tensor imaging [30] in a qualitative agreement with the previous simulation results [21].

4. Discussion

The most general result of this study is the mean frequency offset inside the mesoscopic sphere, Eq. (15). When applied to an experiment, this expression has to be combined with the frequency shift for the specific macroscopic sample shape calculated according to Eqs. (4) and (5) as discussed in Section 3.4. In addition to the magnetic susceptibility tensor, the medium microarchitecture is represented with only five parameters due to the isomorphism

between the elementary dipole field and the spherical harmonics of the order $\ell = 2$.

4.1. Relevant medium parameters and the fate of the Lorentz cavity

The present results contribute to the resolution of the controversy in the literature about the usage of the Lorentz cavity in media with nontrivial microarchitecture [14,10]. The Lorentz cavity is a simplified way to take into account the near field in Eq. (6) by subtracting the field of a cavity of a predefined shape [10], the traditional Lorentz sphere for isotropic media [7,8] or the cylinder for media composed with parallel cylindrical objects [9]. One can hypothesize about an ellipsoid as the interpolating shape. Indeed, the aspect ratios and orientation of an ellipsoid are described by five parameters that might be mapped on the five relevant parameters of the medium magnetic microarchitechture. This is not an easy task though and, moreover, it makes little sense: When the near field is found according to Eq. (15), the problem is already solved in the non-simplified manner. The Lorentz cavity construction is thus abandoned for the direct calculation of the magnetic field in agreement with the recent literature trend [11,21,12,13,32].

To my opinion, the most advanced, but still traditional usage of the Lorentz cavity appears in the calculation of the frequency shift in mixtures of isotropic and long parallel magnetized inclusions with the overall low volume fraction, $\zeta \ll 1$, [11–13]. In these calculations, both inclusion types are assigned the own Lorentz cavity, a spherical and a cylindrical one, respectively. This is justified by the property of the correlation function to be proportional to the sum of correlation functions of different inclusion types when $\zeta \ll 1$. Otherwise, the cross-correlations should be taken into account, which breaks the additivity.

In axially symmetric media, the microarchitecture contributes a single parameter in the frequency shift, the coefficient C_2^0 in Eq. (17). Further parameters of interest are the axial and transverse magnetic susceptibilities, $\chi_\parallel$ and $\chi_\perp$. According to Eq. (18), all three parameters cannot be found from measuring the orientation dependence of the frequency shift. The only available are the products of the magnetic susceptibilities with the microarchitecture-defined coefficient C_2^0.

4.2. Towards realistic model of white matter

Straightforward applications of the present results to brain white matter is hindered by simplifications made in the considered model. The main one is the location-independence of magnetic susceptibility tensor, χ_{ab}. This allowed the factorization of χ_{ab} with the remaining terms giving the pure correlation function, Γ, of the structure, $v(\mathbf{r})$; for the present discussion the notation can be specified as Γ_{vv}. In white matter, such a description can only be applied to the extra-axonal compartment in the idealized case of parallel axons. In the more realistic case of notable orientation dispersion [33–36], the susceptibility tensor follows the orientation of myelinated axons [37,11,21,12,13,38,31]. Extending the present approach to this case requires working with the structure-susceptibility correlation function, $\Gamma_{v\chi}$. While Γ_{vv} can be found using, e.g. electron microscopy [39–41] finding $\Gamma_{v\chi}$ is more difficult because of the need to assign each point a local magnetic susceptibility, which is invisible in histological images. It is also worth noting the nontrivial effect of the radially oriented local magnetic susceptibility of myelin sheets [37,11,13].

Another problem is the multicompartment structure of white matter. At least two compartments, the intra-axonal and extra-axonal water should be taken into account in any measurement. This is possible in principle, but requires further structuring of the correlation functions in intra- and cross-compartmental contributions.

The above problems are not unsolvable, but require further work to create an adequate theoretical description of the phase contrast in brain white matter and perhaps other anisotropic tissues. Even the simplified example considered here shows that the account for microstructure should be essentially more detailed than the simple subtraction of the field of the Lorentz sphere. Neglecting this complexity results in a significant bias when incomplete theory is used for the susceptibility mapping and susceptibility tensor imaging in brain white matter.

Acknowledgments

I am grateful to Kai Zhong and Dmitry S. Novikov for fruitful discussions. This work was partially supported by the German Research Foundation (DFG), grant KI 1089/6-1.

Appendix A. Spherical harmonics of order $\ell = 2$ and a second-rank symmetric trace-free tensor

The second-rank symmetric trace-free tensor is the structure appearing in particular in Eq. (5). Consider a unit three-dimensional vector, $\mathbf{k}$, that can be specified via its Cartesian components, k_a or the two angles of the spherical coordinates, $(k_x, k_y, k_z) = (\sin\theta\cos\varphi, \sin\theta\sin\varphi, \cos\theta)$. Using this relation, it is straightforward to express the spherical harmonics of the second order, $\ell = 2$, in terms of k_a:

$$Y_2^{-2} = \frac{1}{4}\sqrt{\frac{15}{2\pi}}(k_x - ik_y)^2 \tag{A.1}$$

$$Y_2^{-1} = \frac{1}{2}\sqrt{\frac{15}{2\pi}}(k_x - ik_y)k_z \tag{A.2}$$

$$Y_2^{0} = \frac{1}{4}\sqrt{\frac{5}{\pi}}\left(3k_z^2 - 1\right) \tag{A.3}$$

$$Y_2^{1} = -\frac{1}{2}\sqrt{\frac{15}{2\pi}}(k_x + ik_y)k_z \tag{A.4}$$

$$Y_2^{2} = \frac{1}{4}\sqrt{\frac{15}{2\pi}}(k_x + ik_y)^2 \tag{A.5}$$

Solving this system gives the inverse transformation,

$$k_x^2 - \frac{1}{3} = -\frac{2}{3}\sqrt{\frac{\pi}{5}}Y_2^0 + \sqrt{\frac{2\pi}{15}}\left(Y_2^2 + Y_2^{-2}\right) \tag{A.6}$$

$$k_y^2 - \frac{1}{3} = -\frac{2}{3}\sqrt{\frac{\pi}{5}}Y_2^0 - \sqrt{\frac{2\pi}{15}}\left(Y_2^2 + Y_2^{-2}\right) \tag{A.7}$$

$$k_z^2 - \frac{1}{3} = \frac{4}{3}\sqrt{\frac{\pi}{5}}Y_2^0 \tag{A.8}$$

$$k_x k_y = -i\sqrt{\frac{2\pi}{15}}\left(Y_2^2 - Y_2^{-2}\right) \tag{A.9}$$

$$k_x k_z = \sqrt{\frac{2\pi}{15}}\left(Y_2^1 + Y_2^{-1}\right) \tag{A.10}$$

$$k_y k_z = -i\sqrt{\frac{2\pi}{15}}\left(Y_2^1 - Y_2^{-1}\right) \tag{A.11}$$

The quantities on the left-hand sides are the components of the tensor $k_a k_b - \delta_{ab}/3$.

Appendix B. Calculation of $n_a\mathcal{Y}_{ab}\left(\hat{k}\right)\chi_{bc}n_c$ for the case of axial symmetry

It is convenient to work in the eigenvector reference frame of χ_{ab}. The product $n_a\mathcal{Y}_{ab}\left(\hat{k}\right)$ can be calculated explicitly using Eq. (5). The calculation is simplified by omitting all terms of $\mathcal{Y}_{ab}\left(\hat{k}\right)$ that are not contributed by $Y_2^0\left(\hat{k}\right)$ according to Eqs. (A.6)–(A.11); this makes the tensor $\mathcal{Y}_{ab}\left(\hat{k}\right)$ effectively diagonal with the components given by the first terms on the right-hand sides of Eqs. (A.6)–(A.8). It is also convenient to select the direction of the main field in the yz-plane, $\mathbf{n} = (0, \sin\theta, \cos\theta)^\dagger$ in view of the irrelevance of the azimuthal angle in the case of axial symmetry. This gives

$$n_a\mathcal{Y}_{ab}\left(\hat{k}\right) = (0, \mathcal{Y}_{22}\sin\theta, \mathcal{Y}_{33}\cos\theta). \tag{B.1}$$

The remaining factor is simply $\chi_{bc}n_c = \left(0, \chi_\perp\sin\theta, \chi_\parallel\cos\theta\right)^\dagger$. Taking its product with Eq. (B.1) gives

$$n_a\mathcal{Y}_{ab}\left(\hat{k}\right)\chi_{bc}n_c = \mathcal{Y}_{22}\left(\hat{k}\right)\chi_\perp\sin^2\theta + \mathcal{Y}_{33}\left(\hat{k}\right)\chi_\parallel\cos^2\theta. \tag{B.2}$$

Using the explicit form of $\mathcal{Y}_{ab}\left(\hat{k}\right)$, Eq. (5), with the substitution of Y_2^0-proportional terms from Eqs. (A.7) and (A.8) and performing the integration in Eq. (15) using the orthonormality of spherical harmonics results in Eq. (18).

Appendix C. Coefficient C_2^0 for effectively two-dimensional media

The coefficient C_2^0 in Eq. (18) is calculated using the definition given in Eq. (16) and the form of the correlation function, Eq. (21),

$$C_2^0 = \int \frac{dk k^2 d^2\hat{k}}{(2\pi)^3} 2\pi\delta(k_3)\Gamma^{(2d)}(k_1, k_2)Y_2^0\left(\hat{k}\right). \tag{C.1}$$

The three-dimensional integration is restored in this expression. It is therefore convenient to substitute $Y_2^0\left(\hat{k}\right)$ with its form in terms of the Cartesian components of $\hat{k}$, Eq. (A.3). While the presence of $\delta(k_3)$ sets $k_3 = 0$, the two-dimensional correlation function is integrated in the transverse plane according to its relation to the variance of the indicator function and the property $v(\mathbf{r})^2 = v(\mathbf{r})$:

$$\int \frac{\mathrm{d}^2k}{(2\pi)^2}\Gamma^{(2d)}(k) \;=\; \Gamma^{(2d)}(r=0) \;=\; \zeta(1-\zeta). \tag{C.2}$$

This results in Eq. (22).

References

[1] A.M. Abduljalil, P. Schmalbrock, V. Novak, D.W. Chakeres, Enhanced gray and white matter contrast of phase susceptibility-weighted images in ultra-high-field magnetic resonance imaging, J. Magn. Reson. Imag. 18 (3) (2003) 284–290, https://doi.org/10.1002/jmri.10362.

[2] J.H. Duyn, P. van Gelderen, T.-Q. Li, J.A. de Zwart, A.P. Koretsky, M. Fukunaga, High-field MRI of brain cortical substructure based on signal phase, Proc. Natl. Acad. Sci. USA 104 (2007) 11796–11801, https://doi.org/10.1073/pnas.0610821104.

[3] J.P. Marques, R. Maddage, V. Mlynarik, R. Gruetter, On the origin of the MR image phase contrast: an in vivo MR microscopy study of the rat brain at 14.1 T, NeuroImage 46 (2) (2009) 345–352, https://doi.org/10.1016/j.neuroimage.2009.02.023.

[4] H.A. Lorentz, Ueber die Beziehung zwischen der Fortpflanzungsgeschwindigkeit des Lichtes und der Körperdichte, Ann. Phys. 245 (4) (1880) 641–665, https://doi.org/10.1002/andp.18802450406.

[5] W.C. Dickinson, The time average magnetic field at the nucleus in nuclear magnetic resonance experiments, Phys. Rev. 81 (1951) 717–731.

[6] S.C.-K. Chu, Y. Xu, J.A. Balschi, C.S. Springer Jr., Bulk magnetic susceptibility shifts in NMR studies of compartmentalized samples: use of paramagnetic reagents, Magn. Reson. Med. 13 (1990) 239–262, https://doi.org/10.1002/mrm.1910130207.

[7] J. Wolber, A. Cherubini, M.O. Leach, A. Bifone, Hyperpolarized 129Xe NMR as a probe for blood oxygenation, Magn. Reson. Med. 43 (4) (2000) 491–496, https://doi.org/10.1002/(SICI)1522-2594(200004)43:4%3C491::AID-MRM1%3E3.0.CO;2-6.

[8] C.J. Durrant, M.P. Hertzberg, P.W. Kuchel, Magnetic susceptibility: further insights into macroscopic and microscopic fields and the sphere of Lorentz, Concepts Magn. Reson. Part A 18A (2003) 72–95, https://doi.org/10.1002/cmr.a.10067.

[9] X. He, D.A. Yablonskiy, Biophysical mechanisms of phase contrast in gradient echo MRI, Proc. Natl. Acad. Sci. USA 106 (32) (2009) 13558–13563, https://doi.org/10.1073/pnas.0904899106.

[10] D.A. Yablonskiy, X. He, J. Luo, A.L. Sukstanskii, Lorentz sphere versus generalized Lorentzian approach: what would Lorentz say about it?, Magn Reson. Med. 72 (2014) 4–7, https://doi.org/10.1002/mrm.25230.

[11] A.L. Sukstanskii, D.A. Yablonskiy, On the role of neuronal magnetic susceptibility and structure symmetry on gradient echo MR signal formation, Magn. Reson. Med. 71 (2014) 345–353, https://doi.org/10.1002/mrm.24629.

[12] D.A. Yablonskiy, A.L. Sukstanskii, Generalized Lorentzian tensor approach (GLTA) as a biophysical background for quantitative susceptibility mapping, Magn. Reson. Med. 73 (2) (2015) 757–764, https://doi.org/10.1002/mrm.25538.

[13] D.A. Yablonskiy, A.L. Sukstanskii, Effects of biological tissue structural anisotropy and anisotropy of magnetic susceptibility on the gradient echo MRI signal phase: theoretical background, NMR Biomed. 30 (4) (2017) e3655, https://doi.org/10.1002/nbm.3655, NBM-15-0327.R2.

[14] J.H. Duyn, T.M. Barbara, Sphere of Lorentz and demagnetization factors in white matter, Magn. Reson. Med. 72 (1) (2014) 1–3, https://doi.org/10.1002/mrm.25021.

[15] C. Liu, Susceptibility tensor imaging, Magn. Reson. Med. 63 (6) (2010) 1471–1477, https://doi.org/10.1002/mrm.22482.

[16] J. Lee, K. Shmueli, M. Fukunaga, P. van Gelderen, H. Merkle, A.C. Silva, J.H. Duyn, Sensitivity of MRI resonance frequency to the orientation of brain tissue microstructure, Proc. Natl. Acad. Sci. USA 107 (2010) 5130–5135, https://doi.org/10.1073/pnas.0910222107.

[17] P. Sati, P. van Gelderen, A.C. Silva, D.S. Reich, H. Merkle, J.A. de Zwart, J.H. Duyn, Micro-compartment specific T2* relaxation in the brain, NeuroImage 77 (2013) 268–278, https://doi.org/10.1016/j.neuroimage.2013.03.005.

[18] W.C. Chen, S. Foxley, K.L. Miller, Detecting microstructural properties of white matter based on compartmentalization of magnetic susceptibility, Neuroimage 70 (2013) 1–9, https://doi.org/10.1016/j.neuroimage.2012.12.032.

[19] J. Luo, X. He, D.A. Yablonskiy, Magnetic susceptibility induced white matter MR signal frequency shifts–experimental comparison between lorentzian sphere and generalized lorentzian approaches, Magn. Reson. Med. 71 (3) (2014) 1251–1263, https://doi.org/10.1002/mrm.24762.

[20] P. van Gelderen, H. Mandelkow, J.A. de Zwart, J.H. Duyn, A torque balance measurement of anisotropy of the magnetic susceptibility in white matter, Magn. Reson. Med. 74 (5) (2015) 1388–1396, https://doi.org/10.1002/mrm.25524.

[21] S. Wharton, R. Bowtell, Effects of white matter microstructure on phase and susceptibility maps, Magn. Reson. Med. 73 (3) (2015) 1258–1269, https://doi.org/10.1002/mrm.25189.

[22] A. Ruh, H. Scherer, V.G. Kiselev, The Larmor frequency shift in magnetically heterogeneous media depends on their mesoscopic structure, Magn. Reson. Med. 79 (2) (2018) 1101–1110, https://doi.org/10.1002/mrm.26753.

[23] R. Salomir, B.D. de Senneville, C.T.W. Moonen, A fast calculation method for magnetic field inhomogeneity due to an arbitrary distribution of bulk susceptibility, Concepts Magn. Reson. Part B 19B (2003) 26–34, https://doi.org/10.1002/cmr.b.10083.

[24] J.P. Marques, R.W. Bowtell, Using forward calculations of the magnetic field perturbation due to a realistic vascular model to explore the BOLD effect, NMR Biomed. 21 (6) (2008) 553–565, https://doi.org/10.1002/nbm.1224.

[25] A. Ruh, V.G. Kiselev, Larmor Frequency Depends on Structural Anisotropy in Magnetically Heterogeneous Media, ArXiv e-prints arXiv: https://arxiv.org/abs/1808.10171v1.

[26] D.S. Novikov, V.G. Kiselev, S.N. Jespersen, On modeling, Magn. Reson. Med. 79 (6) (2018) 3172–3193, https://doi.org/10.1002/mrm.27101.

[27] K. Zhong, J. Leupold, D. von Elverfeldt, O. Speck, The molecular basis for gray and white matter contrast in phase imaging, Neuroimage 40 (4) (2008) 1561–1566, https://doi.org/10.1016/j.neuroimage.2008.01.061.

[28] Y. Wang, T. Liu, Quantitative susceptibility mapping (QSM): decoding MRI data for a tissue magnetic biomarker, Magn. Reson. Med. 73 (1) (2015) 82–101, https://doi.org/10.1002/mrm.25358.

[29] J.R. Reichenbach, F. Schweser, B. Serres, A. Deistung, Quantitative susceptibility mapping: concepts and applications, Clin. Neuroradiol. 25 (Suppl 2) (2015) 225–230, https://doi.org/10.1007/s00062-015-0432-9.

[30] W. Li, C. Liu, T.Q. Duong, P.C.M. van Zijl, X. Li, Susceptibility tensor imaging (STI) of the brain, NMR Biomed. 30 (4) (2017) e3540, https://doi.org/10.1002/nbm.3540, NBM-15-0287.R1.

[31] J.H. Duyn, Studying brain microstructure with magnetic susceptibility contrast at high-field, NeuroImage 168 (2018) 152–161, https://doi.org/10.1016/j.neuroimage.2017.02.046.

[32] P. Kokeny, Y.-C.N. Cheng, H. Xie, A study of MRI gradient echo signals from discrete magnetic particles with considerations of several parameters in simulations, Magn. Reson. Imag. 48 (2018) 129–137, https://doi.org/10.1016/j.mri.2017.12.019.
[33] T.B. Leergaard, N.S. White, A. de Crespigny, I. Bolstad, H. D'Arceuil, J.G. Bjaalie, A.M. Dale, Quantitative histological validation of diffusion MRI fiber orientation distributions in the rat brain, PLoS One 5 (1) (2010) e8595, https://doi.org/10.1371/journal.pone.0008595.
[34] I. Ronen, M. Budde, E. Ercan, J. Annese, A. Techawiboonwong, A. Webb, Microstructural organization of axons in the human corpus callosum quantified by diffusion-weighted magnetic resonance spectroscopy of N-acetylaspartate and post-mortem histology, Brain Struct. Funct. 219 (5) (2014) 1773–1785, https://doi.org/10.1007/s00429-013-0600-0.
[35] J. Veraart, E. Fieremans, D.S. Novikov, On the scaling behavior of water diffusion in human brain white matter, NeuroImage 185 (2019) 379–387, https://doi.org/10.1016/j.neuroimage.2018.09.075.
[36] B. Dhital, M. Reisert, E. Kellner, V.G. Kiselev, Intra-axonal diffusivity in brain white matter, ArXiv e-printsarXiv: 1712.04565.
[37] S. Wharton, R. Bowtell, Fiber orientation-dependent white matter contrast in gradient echo MRI, Proc. Natl. Acad. Sci. USA 109 (45) (2012) 18559–18564, https://doi.org/10.1073/pnas.1211075109.
[38] J.H. Duyn, J. Schenck, Contributions to magnetic susceptibility of brain tissue, NMR Biomed. 30 (4) (2017), https://doi.org/10.1002/nbm.3546.
[39] R.A. Salo, I. Belevich, E. Manninen, E. Jokitalo, O. Gröhn, A. Sierra, Quantification of anisotropy and orientation in 3d electron microscopy and diffusion tensor imaging in injured rat brain, NeuroImage 172 (2018) 404–414, https://doi.org/10.1016/j.neuroimage.2018.01.087.
[40] A. Abdollahzadeh, I. Belevich, E. Jokitalo, J. Tohka, A. Sierra, 3d axonal morphometry of white matter. bioRxiv: https://doi.org/10.1101/239228.
[41] H-H. Lee, K. Yaros, J. Veraart, J. Pathan, F.-X. Liang, S.G. Kim, D.S. Novikov, E. Fieremans. Electron microscopy 3-dimensional segmentation and quantification of axonal dispersion and diameter distribution in mouse brain corpus callosum. bioRxiv: https://www.biorxiv.org/content/early/2018/06/27/357491.